Space Weather

RESEARCH ARTICLE
10.1029/2020SW002607

Special Section:
Space Weather Events of 4-10 September 2017

Ionospheric Disturbances Over the Indian Sector During 8 September 2017 Geomagnetic Storm: Plasma Structuring and Propagation

L. Alfonsi[1], C. Cesaroni[1], L. Spogli[1], M. Regi[1], A. Paul[2], S. Ray[2], S. Lepidi[1], D. Di Mauro[1], H. Haralambous[3], C. Oikonomou[3], P. R. Shreedevi[4], and A. K. Sinha[5]

[1]Istituto Nazionale di Geofisica e Vulcanologia, Rome, Italy, [2]Institute of Radio Physics and Electronics, University of Calcutta, India, [3]Electrical Engineering Department, Frederick University, Nicosia, Cyprus, [4]School of Space and Environment, Beihang University, Beijing, China, [5]Indian Institute of Geomagnetism, Navi Mumbai, India

Abstract The series of X and M class flares and associated coronal mass ejections that occurred on the first days of September 2017 induced significant perturbations on the low-latitude ionospheric electrodynamics. On 8 September in the Indian sector, the storm caused a severe modification of the equatorial electrojet (EEJ) with a consequent variation of the ionospheric structuring and dynamics. In our analysis, we propose an original method to isolate and identify EEJ variations from geomagnetic data and we detect the presence of equatorial plasma bubbles (EPB) from L-band total electron content (TEC) data in order to understand their movement. Our results provide evidence of independent EPBs appearance freshly generated and inherited from a migrating plasma structure. The EPB (or EPBs) occurring in the south of India is/are freshly generated just above the magnetic equator, and is/are likely triggered by the sudden increase of EEJ just before the local sunset, acting as a pre-reversal enhancement. The EPB appearing in the North-East Indian region is associated with a migrating structure, resulting in a northward movement with a velocity of about 650 m/s, possibly testifying the passage of a large-scale traveling ionospheric disturbance. The occurrence of severe post-sunset scintillations in the northeastern sector suggests a possible cascade process forming small-scale irregularities from the migrating EPB.

Plain Language Summary At low latitudes, the ionosphere, the upper part of the atmosphere rich in free electrons, shows a peculiar distribution of its electron density with two maxima around the geomagnetic equator and a minimum above it. When a geomagnetic storm occurs, this configuration can be deeply modified. The way and the persistence of this modification is a matter of study and, to date, still unpredictable. Our study aims to contribute to the advancement of the knowledge in the field presenting a detailed reconstruction of the ionospheric response over India to the geomagnetic storm occurred in early September 2017. We have detected an uneven distribution of free electrons that shows clear evidence of two deep minima (called bubbles): the first one originated elsewhere and then transported over the considered region, the other one freshly and locally produced. Regional analysis of the ionospheric response to the geomagnetic activity can help to improve the space weather forecasting capabilities, supporting the development of alerts and mitigation tools for the users of communication and navigation systems.

Key Points:

- In the post-sunset hours, the plasma restructuring results into independent equatorial plasma bubbles
- The migrating structure assumed a wave-like pattern possibly related to large-scale traveling ionospheric disturbances moving with a velocity of about 650 m/s
- The method used to derive prompt penetrating electric fields from the overall ionospheric disturbance is able to discriminate between prompt and delayed disturbance

Supporting Information:

Supporting Information may be found in the online version of this article.

Correspondence to:

L. Alfonsi,
lucilla.alfonsi@ingv.it

Citation:

Alfonsi, L., Cesaroni, C., Spogli, L., Regi, M., Paul, A., Ray, S., et al. (2021). Ionospheric disturbances over the Indian sector during 8 September 2017 geomagnetic storm: Plasma structuring and propagation. *Space Weather*, *19*, e2020SW002607. https://doi.org/10.1029/2020SW002607

Received 11 AUG 2020
Accepted 10 FEB 2021

1. Introduction

The low-latitude ionosphere is characterized by the equatorial ionization anomaly (EIA), a local daytime structuring of the plasma forming two electron density maxima (crests) on either sides of the geomagnetic equator (on average at ±15°–20° magnetic latitude [MLAT]), as a consequence of the geometry of the geomagnetic field lines over the equatorial ionosphere coupled with the zonal electric field (McDougall, 1969). During quiet time and at sunset, a rapid rise in the height of the F layer occurs due to the enhancement of the eastward electric field before it reverts to the west. These conditions are those leading to the gravitationally driven Rayleigh-Taylor instability (RTI) at the base of the generation of ionospheric irregularities through the upward **E**×**B** plasma drifts, where **E** and **B** are the electric (eastward) and magnetic (northward) fields at equatorial regions, respectively (Li et al., 2020 and references therein). Ionospheric irregularities refer to an uneven distribution of the electron density resulting into regions of enhanced or depleted

concentration of free electrons. The sizes of irregularities cover a wide range. Generally, at low latitudes smaller scale irregularities (cm to km scale) (Tsunoda, 1980) are embedded into larger structures, known as equatorial plasma bubbles (EPB, 50–1,000 km scale), manifesting as large depletions of electron density (Abdu, 2019 and references therein). Historically, the low latitude small-scale irregularities have been firstly observed as F region echo spreading on ionograms (Booker & Wells, 1938) and, for this reason, some authors refer to them as equatorial spread F (ESF) (Martinis et al., 2005 and references therein). During geomagnetic disturbed conditions, the RTI growth rate can be significantly modified by prompt penetrating electric fields (PPEF) coming from the magnetosphere and by the longer-lived effects due to the thermospheric winds and composition modifications caused by Joule heating in the polar cap (disturbance dynamo electric field [DDEF]) (Fejer, 1991; Prölss, 1995; Shreedevi et al., 2016). In this framework, it is fundamental to investigate the EEJ variations from the local geomagnetic data to learn about the interplay between PPEF and the DDEF. The overall effect of such interplay can lead to a suppression or an increase of post sunset EPBs formation (Scherliess & Fejer, 1997), with a consequent inhibition or exacerbation of ionospheric scintillations (Basu et al., 2001; Biktash, 2004). Storm effects include the appearance of large-scale traveling ionospheric disturbances (LSTIDs), generally caused by traveling atmospheric disturbances (TADs) generated by the sudden Joule heating of the upper atmosphere occurring at auroral latitudes during the storm and mainly due to electric current dissipation (Zakharenkova et al., 2016, and references therein). The effect of geomagnetic storms on the low latitude ionosphere is longitudinally dependent, being strictly correlated to the local time (LT) at which the onset and the main phase of the storm occur (Aarons, 1991; Biktash, 2004). The ionosphere in the Asian sector was significantly affected in the time interval between 7 and 10 September 2017 (Aa et al., 2018, 2019; Jin et al., 2018). Our focus is given to a regional analysis of the ionospheric irregularities appearing at the northern crest of EIA in the Indian sector through the analysis of data acquired by ground based instruments, opportunely combined to provide insight on the local ionospheric response to the storm. In particular, the paper reports the results obtained by using Global Positioning System (GPS) and Global Navigation Satellite System (GNSS) data to reconstruct the TEC and the scintillation variability, and the analysis of ground-based magnetometer data to study the modification of the EEJ. The novel contribution of our work stands in an original method to isolate and identify the EEJ variations from the geomagnetic data and an in-depth analysis of EPB detection and movement from L-band TEC data. Our original approach led to an unprecedented detailed picture of EPB formation and propagation in the considered sector.

2. The Storm on 8 September 2017

In the Sun-Earth interaction, the ionosphere is directly affected by enhanced X-ray and UV radiation flux, mainly occurring during solar flare events, and by the injection of mass and energy from the solar wind following coronal mass ejections (CMEs), which can suddenly modify the electron content leading to the modification of the ionospheric electrodynamics at low latitudes (e.g., Rastogi et al., 1997, 1999; Villante & Regi, 2008). These conditions are monitored by using measurements of the interplanetary magnetic field (IMF) and solar wind (SW) parameters as probed by instrumentation onboard spacecraft in the upstream region, time-shifted to the bow shock nose, provided at 5 min time resolution by OMNI database and available on CDAWeb (https://cdaweb.gsfc.nasa.gov/index.html/). Additional information derived from the measurement of the solar X-ray spectrum in two broad energy bands 1–8 (XL) and 0.5–4 (XS) Å have been provided by the Solar X-ray Sensor (XRS) (Bornmann et al., 1996) at 1 min time resolution, part of the Space Environment Monitor instrumental package, installed on board GOES 13 geosynchronous satellite (https://satdat.ngdc.noaa.gov/).

The geospace conditions in the time interval 4–10 September 2017 are summarized in Figure 1. It shows the SW pressure P_{SW} (panel a) and the radial component of velocity V_{SW} (panel b), the z-component of the IMF (B_z, panel c), the dawn-dusk (y) component of the interplanetary electric field (IEF) computed as $E_y = -V_{SW}B_z$ (panel d) and the X-ray flux (panel e). At ground, the parameters considered here are the equatorial electric field variation (ΔEEF) (panel f), the Sym-H index (panel g) and the AL/AU indices (panel h) provided by the Kyoto World Data Center (http://wdc.kugi.kyoto-u.ac.jp/) at 5-min time resolution; finally, the Joule heating J_h at high latitudes is shown in panel i. In all panels the sunset times at the location and

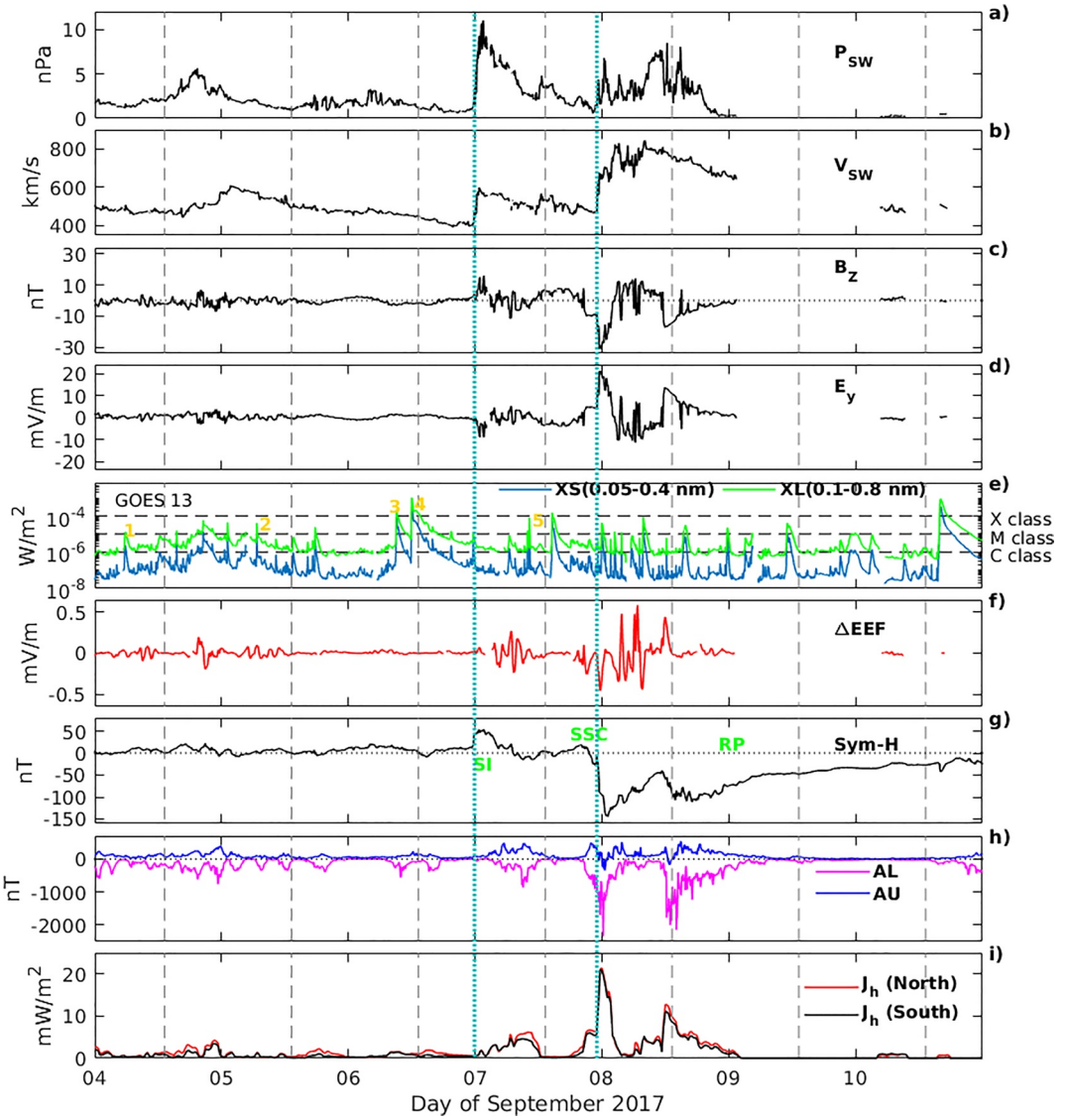

Figure 1. From top to bottom: time series of the solar wind dynamic pressure P_{SW}, panel (a), the radial component of the solar wind velocity V_{SW}, panel (b), the southward interplanetary magnetic field component B_z, panel (c), the duskward component E_y of Interplanetary Electric Field (panel d), solar X-ray fluxes in two broad energy bands 1–8 (XL) and 0.5-4 (XS) Å (panel e), the estimated variations of equatorial electric field adjusted for the local time of Indian sector ΔEEF, panel (f), the Sym-H index (panel g), the auroral indices AL and AU (panel h) and the Joule heating (J_h) estimated for the Northern (red) and Southern (black) polar caps (panel i). Yellow numbers in panel (e) mark solar flares responsible of SFEs in the Indian sector (see Figure 3). The sudden impulse (SI) and the sudden storm commencement (SSC) are marked with cyan vertical lines in all panels; the recovery phase (RP) is also indicated. In all panels the sunset times at the location and days under investigation at 120 km (13:15 UT, ~18:15 LT for the selected sector) are indicated with vertical gray dashed lines.

days under investigation at 120 km (13:15 UT, ~18:15 LT for the selected sector) are indicated with vertical gray dashed lines.

ΔEEF provides a measure of the disturbance to EEF driven by PPEF effect and was estimated by using the empirical model of Manoj and Maus (2012) (see also Manoj et al., 2006, 2008, 2013) by applying a digital filter on E_y measurements and by taking into account the LT scale factor for the Indian sector. The J_h was estimated as the average of the local Joule heating j over the entire polar cap, for each hemisphere. The value of j was computed every 20 min on a grid of 1° latitude × 1° longitude over the polar cap region (from 60°

to 90° N/S) by using the empirical ionospheric dynamic model W05 (Weimer 2005a, 2005b) on 1-h averaged IMF/SW parameters.

The main source of the storm under investigation was the Active Region AR2673, which produced four X-class (X-ray flux $>10^{-1}$ mW/m^2) eruptions with the strongest flare (X9.3) of the solar cycle 24 occurring on 6 September 2017 (number 4 in Figure 1e), and many M-class solar flares (≈40 in total) (Chakraborty et al., 2019). It will be clearly shown in the next sections that only a few solar flares, tagged by sequential yellow numbers in panel e, were able to induce geomagnetic solar flare effects (SFEs) in the Indian sector. During 7–8 September, two CMEs hit the Earth successively triggering a G4 (severe geomagnetic storm – NOAA Kp 8), whose main phase was on 7–8 September 2017 (Linty et al., 2018; Tassev et al., 2017; Vanlommel & Van der Linden, 2017). The IMF B_z component became negative at around 20:40 UT on 7 September and remained southward for about 3 h, and then it rapidly decreased to a minimum of less than −30 nT at 23:31 UT on 7 September. The signatures of the two CMEs are also evident in the increase of the solar wind velocity and pressure. The whole geomagnetic storm is described by the Sym-H behavior, shown in Figure 1g: the event consisted of two sequential storms peaking on September 8, the first with a Sym-H minimum of −146 nT, observed at 01:08 UT, and the second with a broad Sym-H minimum of −112 nT at 17:08 UT. Green labels in Figure 1g mark the following features: the sudden impulse (SI) occurring on 6 September at 23:45 UT, not followed by a geomagnetic storm; the storm sudden commencement (SSC) happening on 7 September at 23:00 UT; the storm recovery phase (RP) following the main phase characterized by the two Sym-H minima over mentioned. The RP, starting at the end (UT) of 8 September, occurred when the B_z was approaching 0 nT after a sequence of oscillations around small, mostly negative, values. The SI and the SSC are marked with cyan vertical lines. From the same figure, a significant auroral activity is observed in the days preceding the storm (AL reached −500 nT several times on September 4), culminating in two AL minima corresponding to the double main phase, testifying the intensification of the auroral electric current system. Such currents result in a significant, quite symmetric, Joule heating of the polar caps.

3. Data and Methods

The regional analysis is based on geomagnetic data recorded by ground-based magnetometers to study the variation of the EEJ and on L-band TEC and scintillation data provided by GNSS receivers to investigate the ionospheric modifications during the storm. The network is reported in Figure 2 and in Table 1, in which the details about the geographic coordinates and the kind of instrument are provided.

In our analysis, we consider the geomagnetic data, provided at 1-min time resolution, acquired by the Indian Institute of Geomagnetism (IIG) by means of the magnetometers located at the equatorial station of Tirunelveli (TIR, quasi dipole [QD] coordinates 1.63°N, 150.38°E) and at the low latitude observatory of Alibag (ABG, QD coordinates 12.69°N, 146.19°E). Beside the geographic coordinates of magnetometers reported in Table 1, we indicate the QD coordinates (Richmond, 1995; VanZandt et al., 1972) which are useful to study phenomena with a specific height distribution, such as ionospheric currents, which are confined to the conducting layer of the ionosphere (see also Laundal & Richmond, 2017). The relative short latitudinal separation (∼11°) and the almost coincident LT of the two considered stations allow separating the geomagnetic signature of the EEJ from that of the solar quiet conditions currents and from the magnetospheric ring currents, as shown by Rastogi and Klobuchar (1990). At both observatories we subtracted to the time series of the horizontal component H its average value computed over the time interval 01–04 LT (supposed to be the quietest geomagnetic time interval in a day) and over the 30 days of September 2017, obtaining the variation ΔH (Figure 3a). Then, in order to identify the EEJ variations, we computed the difference $\Delta(\Delta H) = \Delta H_{TIR} - \Delta H_{ABG}$ (black curve in Figure 3b), which contains mainly the effects of the electrojet current variations due to the ionospheric current system variations and the signature of the geomagnetic SFEs, corresponding to the solar flares marked in Figure 1e and indicated also in Figure 3b. It can be recognized as a regular ("R") variation $\Delta(\Delta H)_R$ with a 1 day periodicity, superimposed on disturbances ("D") so that we can assume

$$\Delta\left(\Delta H\right) \sim \Delta\left(\Delta H\right)_D + \Delta\left(\Delta H\right)_R \quad (1)$$

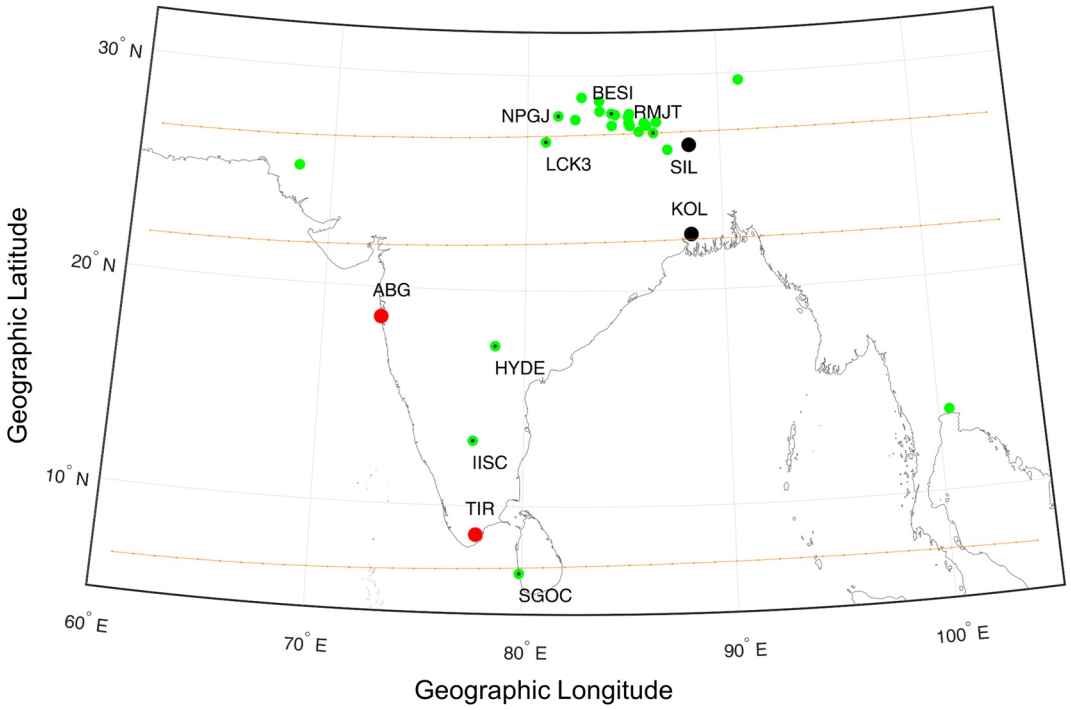

Figure 2. Network of the stations providing the data. Red dots: magnetometers; black dots: scintillations monitors; green dots: GPS stations. In green dots with a black dot inside, a subset of GPS stations used for TIDs detection and ROTI time profiles (see Figure 4). The orange lines represent the position of the dip equator and the isoclinic lines at +15°N and +20°N.

where the disturbance contains the contribution of all ionospheric effects, that is, $\Delta(\Delta H)_D = \Delta(\Delta H)_{DDEF} + \Delta(\Delta H)_{PPEF} + \Delta(\Delta H)_{SFE}$. To remove the contribution of the regular part $\Delta(\Delta H)_R$, we performed a Superimposed Epoch Analysis (SEA) on the 30 days of September, computing both composite mean ($\Delta(\Delta H)_{R,avg}$) and its corresponding standard error of the mean ($SEM_{R,avg}$) which allows identifying the 99% confidence interval as $\Delta(\Delta H)_{R,avg} \pm 2.58\ SEM_{R,avg}$ (Laken & Čalogović, 2013; Regi et al., 2017); this confidence interval is shown as a green strip in Figure 3b. Note that the coefficient 2.58 comes from the assumption that $\Delta(\Delta H)$ follows a Gaussian distribution, as we verified in a separate analysis not shown here. We retain that values of $\Delta(\Delta H)$ lying outside this confidence interval can be interpreted as a reliable alteration of the ionospheric current system above any of the two geomagnetic observatories.

In Equation 1, the disturbed component was first tentatively isolated as $\Delta(\Delta H)_D \sim \Delta(\Delta H) - \Delta(\Delta H)_{R,avg}$ but this time series showed residual fluctuations $\Delta(\Delta H)_{Res}$ showing a 24-h periodicity, probably due to the statistical fluctuations in $\Delta(\Delta H)$ not completely controlled by $\Delta(\Delta H)_{R,avg}$. We isolated these fluctuations through a moving average, acting as a low pass filter, applied to $\Delta(\Delta H) - \Delta(\Delta H)_{R,avg}$, computed over the best estimated window size (Regi et al., 2016) of 12 h.

Then we can assume $\Delta(\Delta H)_R = \Delta(\Delta H)_{R,avg} + \Delta(\Delta H)_{Res}$. Fortunately, regarding $\Delta(\Delta H)_D$, during 7–8 September no remarkable geomagnetic SFEs are found (SFE #5 exhibits a jump of just a few nT), so that for this time interval a disturbance $\Delta(\Delta H)_D \sim \Delta(\Delta H)_{DDEF} + \Delta(\Delta H)_{PPEF}$ can be assumed.

Following all these considerations, equation (1) leads to:

$$\Delta(\Delta H)_D \sim \Delta(\Delta H) - \Delta(\Delta H)_{R,avg} - \Delta(\Delta H)_{Res} \sim \Delta(\Delta H)_{DDEF} + \Delta(\Delta H)_{PPEF} \quad (2)$$

The total electron content (TEC) has been derived from RINEX data provided by GPS receivers covering the region and made available by UNAVCO GAGE Facility archives datasets (Pritchard et al., 2012). The RINEX data are available at a 30 s time resolution. For each satellite-receiver pair, the slant TEC (sTEC) is evaluated by leveraging on the calibration method introduced by Ciraolo et al. (2007) and then evaluating the

Table 1
Identifier, Location, Kind of Instrument and Geographic Coordinates of the Instruments

ID	Location	Instrument	Latitude (°N)	Longitude (°E)
BESI	Besisahar	GPS receiver	28.23	84.38
BRN2	Biratnagar	GPS receiver	26.52	87.27
CHLM	Chilime	GPS receiver	28.21	85.31
CHWN	Chitwan	GPS receiver	27.67	84.39
CUSV	Chulalongkorn	GPS receiver	13.74	100.53
DLPA	Dolpa	GPS receiver	28.98	82.82
DNC4	Dunche	GPS receiver	28.08	85.25
DNSG	Dansing	GPS receiver	28.34	83.76
GRHI	Ghorahi	GPS receiver	27.95	82.49
HYDE	Hyderabad	GPS receiver	17.42	78.55
IISC	Banaglore	GPS receiver	13.02	77.57
JIR2	Jiri	GPS receiver	27.66	86.19
JMSM	Jomsom	GPS receiver	28.81	83.74
KKN4	Kakani	GPS receiver	27.80	85.28
KLCK	Ghorthali	GPS receiver	27.79	86.07
LCK3	Lucknow	GPS receiver	26.91	80.96
LHAZ	Lhasa	GPS receiver	29.66	91.10
LMJG	Lamjung	GPS receiver	28.17	84.57
MUET	Jamshoro	GPS receiver	25.40	68.26
NAST	Patan	GPS receiver	27.66	85.33
NPGJ	Nepalganj	GPS receiver	28.12	81.60
RMJT	Rumjartar	GPS receiver	27.31	86.55
SGOC	Colombo	GPS receiver	6.89	79.87
SNDL	Sindhuli	GPS receiver	27.38	85.80
SYBC	Syangboche	GPS receiver	27.81	86.71
KOL	Kolkata	ISMR	22.58	88.38
SIL	Siliguri	ISMR	26.72	88.39
ABG	Alibag	Magnetometer	18.62	72.87
TIR	Tirunelveli	Magnetometer	8.67	77.81

corresponding vertical TEC by applying a mapping function as described in Mannucci et al. (1998). For the remainder of the paper, we refer to the vertical TEC simply as TEC. By this application, a thin-shell model of the ionosphere is assumed, whose altitude is set at 350 km, being a good approximation of the height of the F-layer peak density. In addition, only observations with an elevation mask greater than 30° have been considered. For mapping purposes, we integrate TEC measurements at the different ionospheric pierce points (IPPs), assumed to be located at the same height of the single ionospheric layer, by applying the natural neighbors interpolation (Okabe et al., 1994) on a 1° latitude × 1° longitude grid. Such approximation has been proven to provide a more realistic representation of the TEC behavior with respect to other methods (see, e.g., Cesaroni et al., 2015 and references therein). To obtain the TEC maps, the measurements are integrated over a time window of 15 min, in which the low-latitude ionosphere is reasonably assumed to be frozen. We also derive from TEC maps the corresponding maps of meridional (TECgradN) and zonal TEC gradients (TECgradE), according to Equations 4 and 5 of Cesaroni et al. (2015).

Additionally, to provide a measure of the signal fluctuations triggered by the presence of ionospheric irregularities, we also evaluated the rate of TEC change (ROT) index (ROTI) for each satellite-receiver pair having elevation larger than 30° and for 5-min intervals (Pi et al., 1997). ROTI is defined as the standard deviation of ROT, that is:

$$\mathrm{ROTI} = \sqrt{\langle \mathrm{ROT}^2 \rangle - \langle \mathrm{ROT} \rangle^2}, \tag{3}$$

in which the brackets indicate the time average over the 5-min window and ROT is the sTEC time derivative between two epochs, namely t_i and t_{i-1}, according to the following:

$$\mathrm{ROT} = \frac{\mathrm{sTEC}_i - \mathrm{sTEC}_{i-1}}{t_i - t_{i-1}}. \tag{4}$$

Values of ROTI above a threshold of 0.5 TEC/minute are used to identify ionospheric irregularities with a typical scale size of a few kilometers and above (Alfonsi et al., 2011; Ma & Maruyama, 2006; Yang & Liu, 2016).

The picture about the formation of ionospheric irregularities is completed through the amplitude scintillation data acquired by the Ionospheric Scintillation Monitor Receivers (ISMRs) located in Kolkata e Siliguri (black dots in Figure 2). The receiver in Kolkata (KOL) is a Novatel GSV4004B GPS Ionospheric Scintillation and Total Electron Monitor (GISTM). It is capable of computing, from 50 Hz samples, the amplitude and the phase scintillation indices on the GPS L1 (1,575.42 MHz) signal and on those transmitted by available geostationary satellites of the Satellite-Based Augmentation Systems (SBAS) (Van Dierendonck et al., 1993). The receiver in Siliguri (SIL) is a PolaRxS receiver, which provides multi-constellation tracking ability (Bougard et al., 2011). Similar to GSV4004, it provides phase and amplitude scintillation indices from 50 or 100 Hz sampling of the GNSS signals, but for all the frequencies and constellations, including SBAS satellites. In the present analysis, it was set to acquire GPS, GLONASS, Galileo and SBAS signals at a 50 Hz sampling rate. Both ISMRs are owned by the University of Kolkata and more detailed information on these systems and stations are available in the literature (Goswami et al., 2018 and references therein).

For the purpose of this paper, we concentrate solely on the amplitude scintillation index S4, that is defined as the standard deviation of the normalized signal intensity (Fremouw et al., 1978). Despite the different number of receivers used for ROTI (25) and for S4 (2) calculations, and the fact that the different coverage

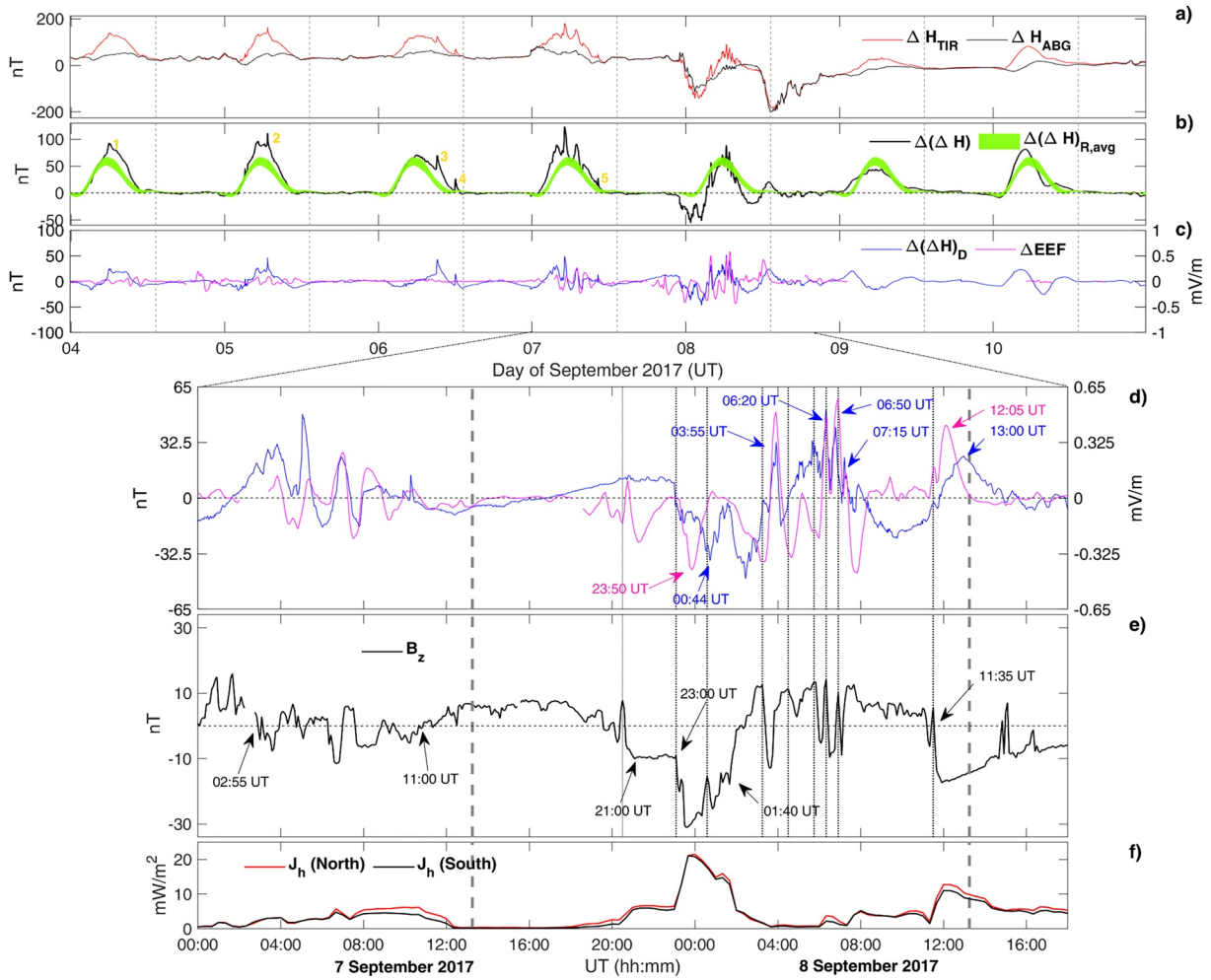

Figure 3. Geomagnetic horizontal field variations ΔH at ABG and TIR (panel a); difference between horizontal field variations at ABG and TIR (black curve) together with its average regular variation (green strip, indicating the 99% confidence interval) (panel b); equatorial electric field variation (magenta curve) and disturbed part of the difference between horizontal field variations at ABG and TIR (blue curve) (panel c). Yellow numbers in panel (b) mark geomagnetic SFEs (see Figure 1e): in the range 7 September 00:00 UT to 8 September 18:00 UT, zoom of the plots in panel (c), of the southward Interplanetary Magnetic Field component B_z (Figure 1c) and of the Joule heating (Figure 1i). The vertical gray dashed lines indicate the sunset time at 120 km. Vertical black dotted lines indicate the timing of the main B_z turnings.

limits the possibility of a thorough integration, the joint use of ROTI and S4 allows speculating on the scale sizes of the irregularities during the storm. ROTI is more sensitive to large-scale depletion changes (above few kilometers), while S4 index is sensitive to small-scale ones, that is, those below the Fresnel's frequency for L-band signals, being of the order of a few hundreds of meters (see, e.g., Ghobadi et al., 2020 and references therein). Usually when small-scale irregularities exist and trigger scintillation, they are formed in the plasma cascade from large-scale plasma structures, typically EPBs. So the combined investigation of ROTI and S4 should account for the cascading process.

Another typical phenomenon of the perturbed ionosphere is the occurrence of wave-like perturbations, possibly identified as traveling ionospheric disturbances (TIDs). To identify such wave-like perturbations, we used the VARION algorithm described in Savastano et al. (2017) and Ravanelli et al. (2020). This approach is able to identify wave-like perturbations in the ionosphere by calculating the integral over a certain period of time of the time differences of geometry-free combinations of carrier-phase measurements from a stand-alone GPS station, according to the following:

$$\Delta \mathrm{TEC}_{\mathrm{VAR}}\left(t\right) = \int_{t_i}^{t} \delta \mathrm{TEC}\left(t'+1,t'\right)dt' = \int_{t_i}^{t}\left[40.3\left(\frac{1}{f_2^2}-\frac{1}{f_1^2}\right)\right]^{-1}\left(L_{4R}^{S}\left(t'+1\right)-L_{4R}^{S}\left(t'\right)\right)dt' \quad (5)$$

where t_i represents the initial time of the considered period, L_{4R}^{S} is the geometry free combination of the carrier phase measurements calculated considering the receiver R and the satellite S and f_1 ,f_2 are the GPS L1 and L2 signal frequencies, respectively.

The algorithm makes use of the standard orbit and clock products and assumes a thin layer approximation, located at 350 km. Time differencing of the carrier phase measurements allows ignoring the effect of the inter-frequency biases on TEC evaluation, since they can be considered constant along each single arc, if no cycles slips occur. In order to remove the long-term trend from $\Delta \mathrm{TEC}_{\mathrm{VAR}}$ time series, the residuals with respect to a tenth order polynomial fit are calculated.

Time series of $\Delta \mathrm{TEC}_{\mathrm{VAR}}$ obtained from the meridional chain of receivers which includes NPGJ, LCK3, IISC, HYDE, and SGOC receivers (Figure 2) are used to evaluate the possible presence of wave-like propagation in the ionosphere. A cross-correlation analysis applied to such time series is used to provide a measure of the meridional velocity of the perturbation.

4. Results

Figure 3 shows ΔH at both observatories (panel a), while $\Delta(\Delta H) = \Delta H_{TIR} - \Delta H_{ABG}$ which contains mainly the effects of the electrojet current variations is shown in panel b (black curve), together with $\Delta(\Delta H)_{R,avg}$ (green strip). In panel c, the expected ΔEEF (purple) and estimated $\Delta(\Delta H)_D$ (blue) are compared.

A zoom of the panel c in the range 7 September 00:00 UT to 8 September 18:00 UT is provided in panel d, and corresponding zoom of the IMF B_z and of J_h are given in panels e and f, respectively.

The vertical gray dashed lines indicate the sunset time at 120 km at 13:15 UT (~18:15 LT for TIR-ABG). The yellow numbers in panel b mark the geomagnetic SFEs, already reported in Figure 1.

In the early UT hours of 7 September, ΔEEF fluctuations are in phase with those observed in the $\Delta(\Delta H)_D$, indicating that probably the main disturbance came from PPEF. This is confirmed by the B_z sudden flips between positive and negative values from 02:55 UT to 11:00 UT of 7 September (Figure 3e). Conversely, late on 7 September and in the first half of 8 September different effects can be observed from Figures 3b–f:

During 18:00–15:00 UT (corresponding to ~ 23–20 LT) fluctuations of both ΔEEF and $\Delta(\Delta H)_D$ are not always in agreement, likely indicating the interplay between PPEF and DDEF effects on EEJ intensity variations. In this time range, main PPEF events (those with full agreement between ΔEEF and $\Delta(\Delta H)_D$) peak during local daytime, specifically at 03:55 UT, 06:20 UT, 06:50 UT, and 07:15 UT on 8 September. Delayed effects of B_z turning on $\Delta(\Delta H)_D$ are probably due to the DDEF contributions as the cases at 00:44 UT of 8 September (following the 23:50 ΔEEF negative peak) and at 13:00 UT (following the 12:05 UT ΔEEF positive peak). DDEF effects are probably linked to the J_h enhancement starting about a couple of hours in advance (Figure 3, panel f). Among the enhanced J_h, the most relevant occurred at 23:40 UT on 7 September (starting at about 23:00 UT) and 12:00 UT on 8 September (starting at about 11:20 UT).

From ~23:00 UT (04:00 LT) until ~04 UT (~09 LT) and from ~08:00 UT (13:00 LT) until ~12:00 UT (~17 LT), we clearly observe that Δ(ΔH) is well below its corresponding reference confidence interval (Figure 3b), corresponding to definitely negative $\Delta(\Delta H)_D$ (Figure 3d), indicating the occurrence of two counter electrojets (CEJs). The first one, characterized by two negative peaks (at 00:44 UT and 02:27 UT on 8 September), starts at 23:00 UT on 7 September, i.e. during local night-time (04:00 LT) on 8 September. This is triggered by the sudden negative variation of B_z (from −10 nT to −30 nT), which causes a westward PPEF event (negative ΔEEF), peaking at 23:50 UT (04:50 LT) and driving mainly the CEJ peak at 00:44 UT. Conversely, the following B_z steep positive variation (from −18 to 12 nT) starting at 01:40 UT (06:40 LT) on 8 September, occurs during local daytime. This leads to overshielding PEFs that are westward in the dayside (Abdu, 2012) and that are the main cause of the CEJ peak at 02:27 UT. The second CEJ, peaking at 09:40 UT on 8 September, does not agree with expected ΔEEF,

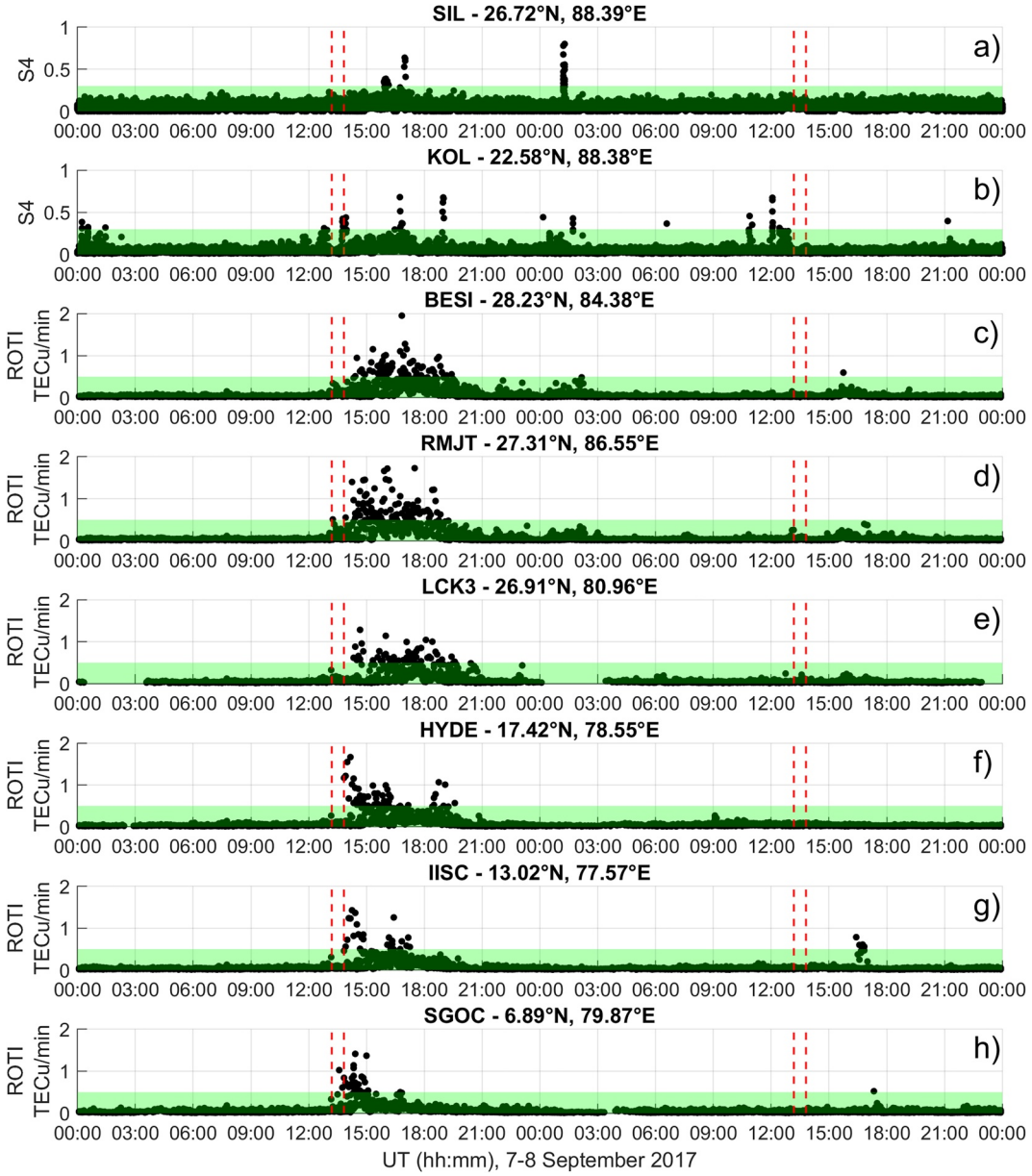

Figure 4. Time profiles of S4 (a–b) and of ROTI (c–h) obtained by considering all satellite in view from the station indicated in each panel during seven and 8 September. The red-dashed lines indicate the time of the passage of the Sun terminator at the station location and at an altitude of 120 km and of 350 km. The green shaded area indicates the ranges S4 < 0.3 and ROTI < 0.5 TECu/min.

indicating the action of DDEF. This CEJ is followed by an enhanced EEJ (indicated by Δ(ΔH) being considerably higher that its reference confidence interval and corresponding to positive $\Delta(\Delta H)_D$) with maximum values at 13:00 UT (~18 LT) vanishing after the PRE at ~14:08 UT. This EEJ enhancement acts as a PRE, as it peaks right before the passage of the sunset terminator (gray dashed lines). Thus, the geomagnetic storm is able to generate such a PRE, that acts as a seed for EPB, as discussed further in the following sections.

Figure 4 reports the time profiles of S4 (panels a and b) and of ROTI (panels c to h) obtained by considering all satellites in view from the selected stations (indicated in each panel) during 7 and 8 September. The selected stations operate the scintillation monitors and other GNSS receivers forming a quasi-meridional chain (apart from RMJT). The red-dashed lines indicate the time of the passage of the solar terminator at

the station location at an altitude of 120 and 250 km, assumed to be representative of E-layer and F-layer peak heights, respectively. This twofold representation of the terminator is due to the fact that mechanisms justifying the PRE enhancement involve the electrodynamics of both E- and F-layers, even if favoring those related to F-layer (Eccles et al., 2015). The ROTI (panels c to h) starts enhancing right after the passage of the terminator at the F-layer altitude (~13:50 UT), indicating the presence of large-scale irregularities embedded in the EPBs. As expected the ROTI time profiles of BESI, RMJT and LCK3 behave in a similar way, presenting a broad peak of ROTI fading out at ~18:45UT. ROTI enhancements have a delay of some minutes as noted at BESI (~14:30 UT), RMJT (~14:15 UT) and LCK3 (~14:25 UT) with respect to the time of the terminator, possibly indicating that the EPB causing the ROTI enhancement is not freshly generated in that latitudinal sector, but likely a migration of an EPB from other geographical sectors. The reported terminators are taken at the station overhead, while in theory one should consider the time of the terminator with respect to the location of each IPP. Bearing this in mind, the fact that the EPB seen at higher latitudes is not freshly generated there seems to be confirmed by looking at ROTI time profiles of SGOC (panel h), IISC (panel g) and HYDE (panel f), for which the ROTI enhances exactly in correspondence with the terminator. In addition, the ROTI peak is more confined in time with respect to the higher latitudes, reinforcing the idea of the presence of another EPB (or probably of other EPBs) freshly generated not far from the magnetic equator. In order to study the small-scale irregularities that may form in the plasma cascade featuring the EPB space-time evolution, the S4 presents an almost simultaneous narrow peak at both SIL and KOL stations at about 17:00 UT on 7 September, which is in agreement with the maximum ROTI activity at both BESI and RMJT, being two closely located stations. During the same (UT) day, a second pronounced peak at KOL is present at 19:00 UT that seems to correspond with the ROTI enhancement roughly at the same times at BESI, RMJT and LCK3. No similar S4 enhancement is found at SIL, likely indicating that the formation of this second structure of small-scale irregularities is not able to map over SIL. Some other peaks of S4 are present on 8 September at both SIL and KOL, but the absence of a corresponding ROTI enhancement suggests that they are likely due to instrumental issues.

To better draw the picture of the latitudinal behavior of the small- and large-scale irregularities during the storm and relate it with TEC variations, panel a of Figure 5 shows the keogram of the TEC difference between 8 September and a quiet time reference as a function of time and latitude. To identify such quiet reference, the following has been taken into account:

- To minimize the effect of the day-to-day variability of the low-latitude ionosphere and to consider similar solar flux and seasonal conditions, the period between 1 August and 30 September 2017 has been taken into account;
- Among the days of that period, days characterized by quiet geomagnetic conditions (Dst > -35 nT) and low auroral activity (AE<400 nT) are selected.

According to this criterion, the following days are considered for the quiet time reference: 15, 16, 26, 28 August and 25 and 26 September 2017.

Green diamonds represent the time and the latitude of IPPs having ROTI>0.5 TECu/min, while black dots are for IPPs having S4>0.3. For both ROTI and S4, the dimension of the marker is proportional to the corresponding value. The orange dashed lines indicate the position of the magnetic equator and of the isoclinic lines at +15° and +20°, as an average indication of the EIA northern crest. The blue dashed lines indicate the time of the solar terminator at (24°N; 88°E), at an altitude of 120 and 350 km, assumed to be representative of E-layer and F-layer peak heights. The plot is obtained by considering all the GNSS receivers reported in Figure 2 and Table 1. S4 increases within the crest between about 15:30 UT and 17:00 UT. Another S4 enhancement is found at around 16:30-17:00 UT, but displaced equatorward (between 16°N and 18°N). As already noticed in panels a and b of Figure 4, a secondary scintillation activity is detected at a later time (19:00 UT on 7 September) at around 20°N. It is also worth noticing that S4 enhancements occur in correspondence with the larger values of ΔTEC found in the ISMRs' field of view. In addition, the ΔTEC keogram reveals the daytime effect of the strong CEJ conditions (middle panel of Figure 3). Specifically, the CEJ conditions result in a depleted $|\mathbf{E}\times\mathbf{B}|$, which limit the uplift of the ionospheric F-layer in the noon and afternoon sectors. Consequently, the northern crest of the EIA is displaced equatorward resulting in a single broad TEC increase around the dip-equator and a decrease of TEC at about 15° MLAT (about 24°N),

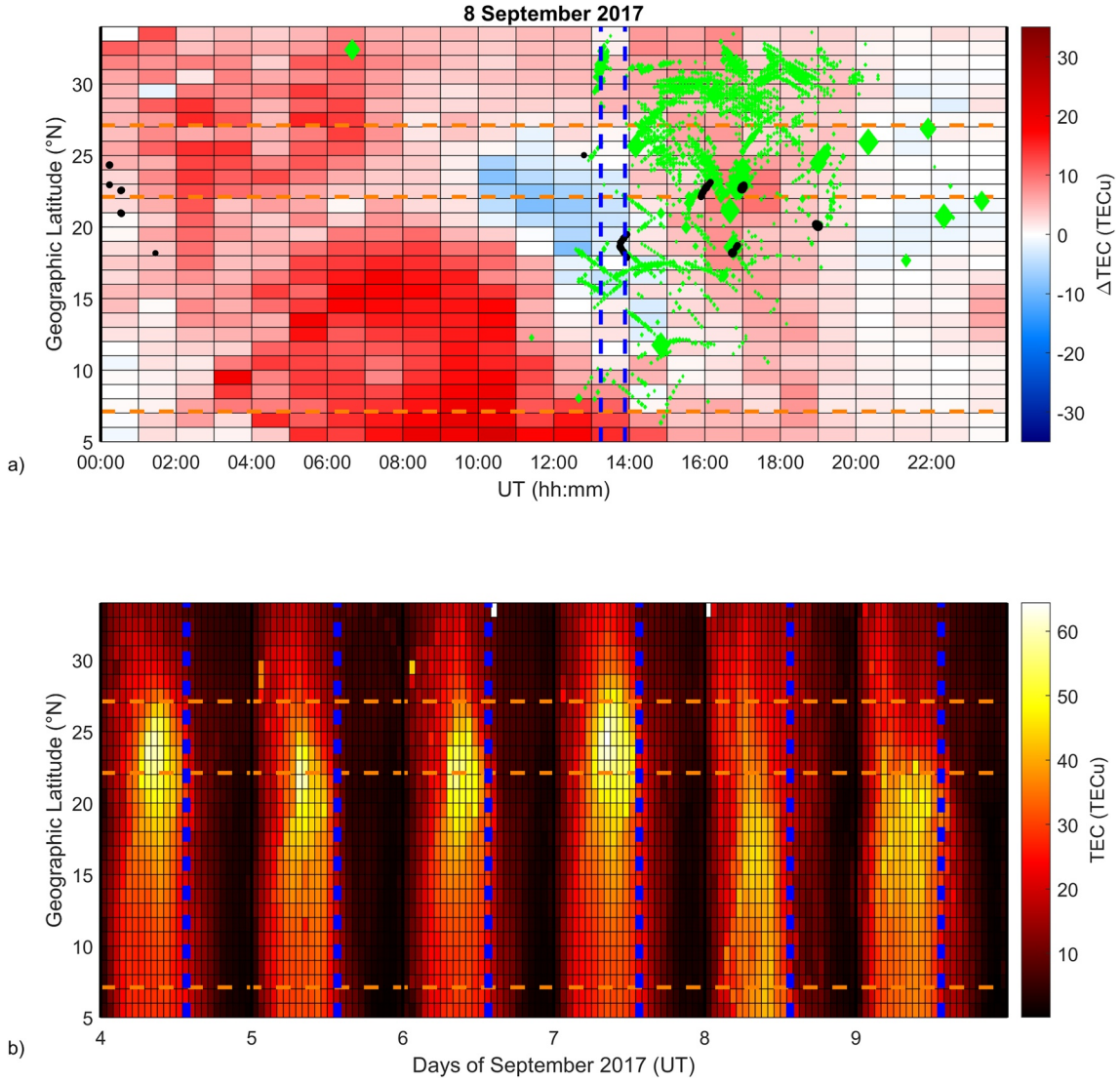

Figure 5. (Panel a) Keogram showing the TEC difference between 8 September and quiet reference as a function of time and latitude. Green diamonds represent the time and latitude of IPP having ROTI>0.5 TECu/min, while black dots are for IPP having S4>0.3. For both ROTI and S4, the dimension of the marker is proportional to the corresponding value. (Panel b) Keogram showing the absolute TEC in the period 4–9 September 2017. In both panels, the orange dashed lines indicate the position of the magnetic equator and of the isoclinic lines at +15° and +20°. The blue dashed lines indicate the time of the solar terminator at (24°N; 88°E) and at an altitude of 120 and 350 km, assumed to be representative of E-layer and F-layer peak heights. In panel b, the time difference between the two solar terminator times is not resolved.

right before the passage of the solar terminator. This is also clearly visible in Figure 5b, which reports the keogram of absolute TEC in the period 4–9 September 2017.

To better investigate the two plasma structures (migrating and freshly generated EPBs) concurring to the irregularity pattern found in the considered area, Figure 6 reports the maps of TEC (left column), TECgradN (middle column) and TECgradE (right column) at each hour between 13:00 UT and 19:00 UT on 8 September. Each map is obtained by considering 15 min of data (e.g., from 13:00 to 13:15 UT). Black diamonds represent the time and latitude of IPPs having ROTI>0.5 TECu/min, while blue dots are for IPPs having S4>0.3. For both ROTI and S4, the dimension of the marker is proportional to the corresponding value. In the supporting information, the same maps, but obtained with a time step of 5 min and between 12:30 UT and 19:30 UT, are also reported to provide a picture with a finer time resolution. Before 12:55 UT, no ROTI enhancements above 0.5 TECu/min are present. From the maps, the two regions observing different EPBs are highlighted. To be specific, the migrating TEC depletions and related ROTI enhancements appear since

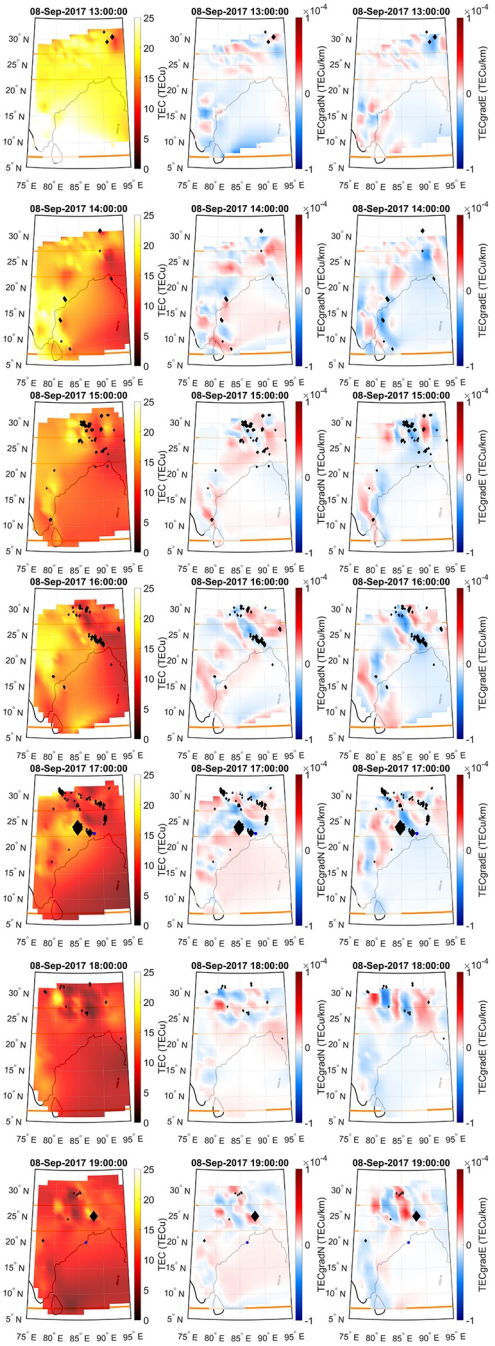

Figure 6. Maps of TEC (left column), TECgradN (middle column) and TECgradE (right column) at each hour between 13:00 UT and 19:00 UT on 8 September. Each map is obtained by considering 15 min of data (e.g., from 13:00 to 13:15 UT). Black diamonds represent the time and latitude of IPP having ROTI>0.5 TECu/min, while blue dots are for IPP having S4>0.3. For both ROTI and S4, the dimension of the marker is proportional to the corresponding value. The orange lines represent the position of the dip equator and the isoclinic lines at +15° and +20°.

13:00 UT in the North-East sector and drift westward. We remind here that the ionosphere over the northern Indian sector is well characterized by the dense network of GPS receivers, located close to the Tibetan plateau (Figure 2 and Table 1). The migrating bubble is well depicted in the maps related to 17:00 UT in terms of TEC depletion (down to 7 TECu) and of both TECgradE and TECgradN negative values. Also the ROTI enhancements allows the identification of the migrating EPB by drawing the boundaries at which the largest TEC gradients are found. The largest ROTI values are found at about 24°N, together with presence of small scale irregularities formed in the plasma fragmentation and revealed by S4 (blue dots in the map). The freshly generated EPB (or EPBs) appears in the Southernmost part of the maps in Figure 6 starting from 14:00 UT. The lower coverage of GPS receivers in Southern India and Sri Lanka regions does not allow to resolve the EPB with the same level of detail of the migrating one. In addition, no ISMR data are available in the region and, consequently, we cannot investigate if small-scale irregularities form from the freshly formed EPB(s). The TEC depletion and the TEC spatial gradients resulting in ROTI enhancements in the southernmost region cover the time window between 13:35 UT and 15:10 UT.

The top and middle panels of Figure 7 and Figure 8 show the time series of ΔTEC_{VAR} of the pair NPGJ and LCK3 and of the pair LCK3 and HYDE (quasi-meridionally distributed) between 14:30 UT and 15:45 UT on 8 September for PRN18. In the bottom panels the corresponding cross-correlation coefficient between −45 and + 45 min is reported, while the distance between the IPPs of PRN18, related to the different stations at the same time, is provided as a function of time. The quasi-periodical behavior of the correlation coefficients follows from the wave-like nature of the ΔTEC_{VAR} and allows to estimate its period as about 25 min (corresponding to 50 time steps). From both the station pairs the mean propagation velocity can be derived from the ratio between the time lag corresponding to the maximum correlation coefficient and the mean distance of the IPPs. By considering the variation of the IPPs' distance during the selected period, the uncertainty on the velocity can be calculated as the maximum semi-dispersion:

$$\Delta v = \frac{1}{2}\left(\frac{D_{\max}}{T} - \frac{D_{\min}}{T}\right) \tag{6}$$

where $D_{max}\left(D_{\min}\right)$ is the maximum (minimum) distance of the IPPs during the considered period and T is the maximum correlation lag (here assumed without uncertainty). The results are reported in Table 2.

5. Discussion

The geomagnetic time series data collected at TIR and ABG allow examining EEJ variations during disturbed magnetospheric conditions. In this regard, the solar wind transfers its energy to the ionosphere system mainly through interplanetary-magnetospheric magnetic field coupling process, leading to PPEF acting on 7 September 2017.

The physical system becomes more complex during 7–8 September when:

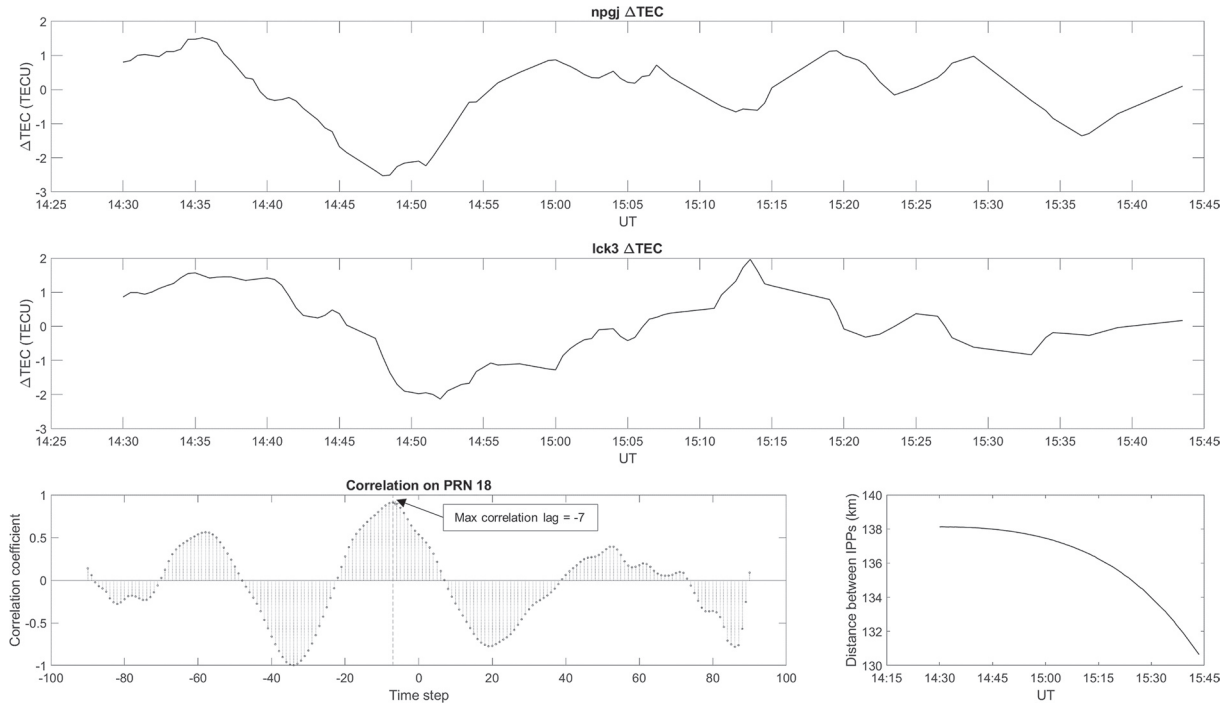

Figure 7. Time series of ΔTEC_{VAR} from NPGJ (top) and LCK3 (middle) between 14:30 UT and 15:45 UT on 8 September for PRN18. (bottom left) Corresponding cross-correlation coefficient between -45 and + 45 min corresponding to −90 and 90 ΔTEC timestep (30 s), respectively. (bottom right) distance between IPP of PRN18 as seen from NPGJ and LCK3 as a function of time.

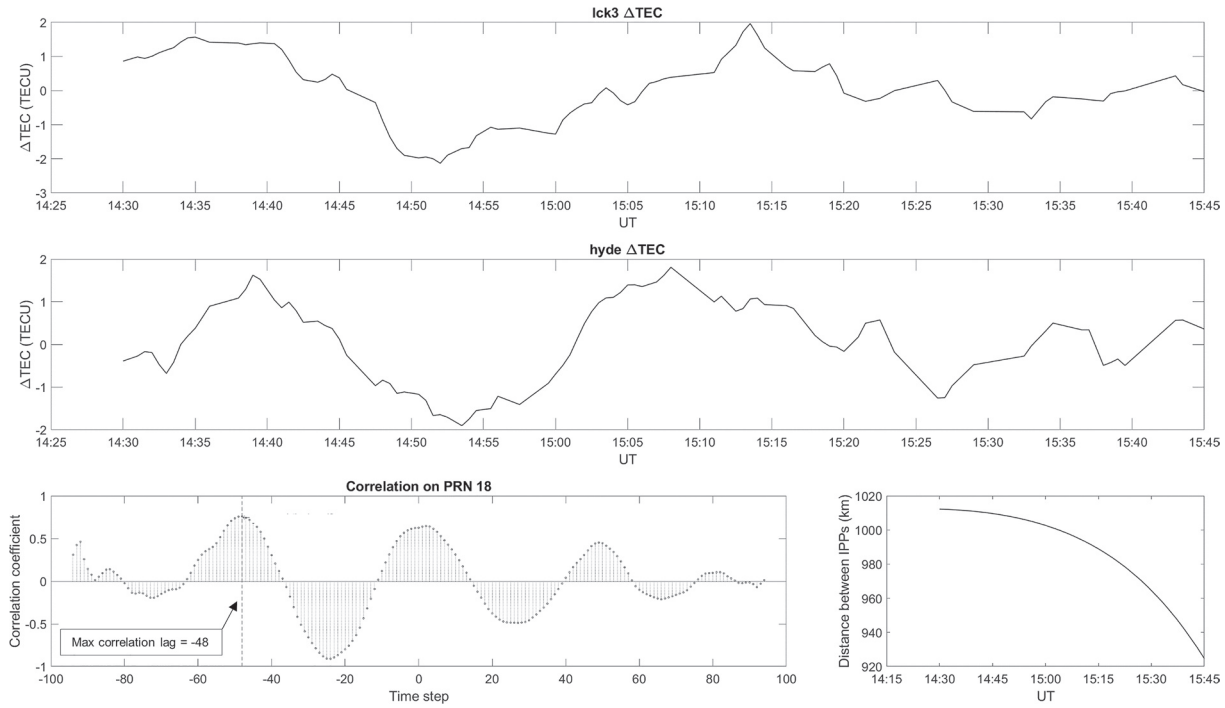

Figure 8. Time series of ΔTEC_{VAR} from LCK3 (top) and HYDE (middle) between 14:30 UT and 15:45 UT on 8 September for PRN18. (bottom left) Corresponding cross-correlation coefficient between −45 and + 45 min corresponding to -90 and 90 ΔTEC timestep (30 s), respectively. (bottom right) distance between IPP of PRN18 as seen from LCK3 and HYDE as a function of time.

Table 2
Mean Velocities and Corresponding Maximum Semi-dispersion Evaluated From the Considered GNSS Station Pairs

Station pairs	Mean velocity (m/s)	Δv (m/s)
NPGJ-LCK3	638	19
LCK3-HYDE	670	31

(i) Two CEJ events happen: the first starts at 23:00 UT on 7 September and has 2-peaks shape (00:44 UT and 02:27 UT on 8 September), while the second starts at 08:08 UT on 8 September and peaks at 09:40 UT;
(ii) A sudden increase of EEJ occurs just before the local sunset, whose peak is at 13:00 UT on 8 September.

The PPEF event causing the CEJ conditions starting at 23:00 UT on 7 September follows from the abrupt decrease of the IMF B_z (up to about −30 nT) from steady negative B_z conditions (about −10 nT) lasting from 21:00 UT to 23:00 UT and causing the westward PPEF event, whose peak is at 23:50 UT, as expected by undershielding conditions during local nighttime. Conversely, the following PPEF event is triggered by the negative to positive turning of the IMF-B_z starting at 01:40 UT on 8 September, which causes overshielding conditions during local daytime, again resulting in a westward disturbance to the EEF and consequent CEJ conditions.

The second CEJ, starting at 08:08 UT and peaking at 09:40 UT of 8 September, is triggered by DDEF resulting as a consequence of a long lasting positive IMF B_z. Moreover, the subsequent increase of EEJ before sunset (peaking at 13:00 UT) confirms the presence of PPEF which has an eastward polarity in the dusk sector (peaking at 12:05 UT). This is due to the sudden southward turning of IMF B_z occurring at 11:35 UT (Figure 3e). It is more likely that the sudden increase of EEJ and the subsequent post-sunset EPBs event are the result of eastward PPEF which counteracts and reverses the effect from the westward DDEF. This EEJ enhancement occurs in correspondence with the expected time of a PRE. Indeed, our results provide clear evidence of EPBs appearance on the 8th of September in India. Our detailed analysis reveals that the EPBs appearing after sunset in the north-east and south part of the considered region are independent: the first EPB derives from a migrating TEC depletion moving westward, the other EPB (possibly EPBs) is freshly generated just above the magnetic equator. The cross-correlation analysis of the TEC perturbations recorded by two pairs of GNSS stations quasi-meridionally oriented suggests that the detected migrating TEC structure moves northward with a wave-like propagation. The same analysis suggests the possible presence of LSTIDs or of an EPB moving at about 650 m/s. The presence of LSTIDs could be due to the enhanced auroral activity around noon inducing Joule heating (Figure 1). The estimated velocity of the LSTID is compatible with a TAD in the polar cap reaching India in about 2.5 hours. The migration of the EPB confirms what was found by Aa et al. (2018) reporting the observation of super plasma bubbles in the evening sector within China and adjacent areas moving northwestward. The velocity estimated by these authors (Aa et al., 2018) was around 800 m/s, in good agreement with our findings. The small-scale irregularities, likely produced through a cascading process from the migrating EPB, triggered scintillations in the evening hours over Kolkata and Siliguri. The freshly generated EPB located in the southern sector is reported for the first time in our analysis. This is likely generated locally due to the EEJ enhancement occurring just before the PRE. Unfortunately, the scarce coverage of GNSS receivers and the lack of scintillation data availability in the southern sector does not allow further investigation.

6. Summary and Conclusions

The geospace response to the storm which occurred in early September 2017 has been extensively studied at global and regional level. In this paper we focus on the ionospheric perturbations recorded in the Indian sector as the result of the disturbed EEJ on the modification of the plasma structuring and dynamics. From our in-depth analysis of the modifications observed on 8 September we can conclude that:

1. The sudden increase of EEJ (peaking at 13:00 UT on 8 September, i.e., 18:00 LT), induced by a southward turning of B_z causing an enhancement of E_y, acts as a PRE and seed for the EPBs formation.
2. In the post-sunset hours of 8 September, the plasma restructuring results into two independent groups of EPBs. The one appearing in the north-east Indian region is associated with a migrating westward structure, while the other occurring in the south is freshly generated just above the magnetic equator.
3. The migrating structure assumed a wave-like pattern possibly related to LSTIDs moving northward with a velocity of about 650 m/s and a period of about 25 min.

4. The combination of the aforementioned results confirms the presence of plasma structures moving northwestward.
5. The method here used to identify DDEFs and PPEFs from the overall ionospheric disturbance is promising to discriminate the prompt and delayed disturbance impacts on the low latitude electrodynamics.

Data Availability Statement

The magnetometer and scintillation monitor data supporting the conclusions are available through this link: https://www.dropbox.com/sh/egb0uldqmn88o2a/AAB6138C6IObeaXob0jtNjcsa?dl=0.

Acknowledgments
This work has been carried out as part of the International Space Science Institute (ISSI) project "Multi-technique Characterization of Near-Earth Space Environment" led by Prof. Ashik Paul, Institute of Radio Physics and Electronics, University of Calcutta. The material used in the paper is based on services provided by the GAGE Facility, operated by UNAVCO, Inc., with support from the National Science Foundation and the National Aeronautics and Space Administration under NSF Cooperative Agreement EAR-1724794. The interplanetary magnetic field and solar wind data are provided by Coordinated Data Analysis Web (CDAWeb, https://cdaweb.sci.gsfc.nasa.gov). The Sym-H data are provided by the World Data Center for Geomagnetism, Kyoto (http://wdc.kugi.kyoto-u.ac.jp/). The authors also thank the principal investigators and teams of the X-ray flux experiments on GOES 13 satellite (https://satdat.ngdc.noaa.gov/) and Daniel Weimer at Space Science Center and Engineering Research (Virginia Tech) who provided the ionospheric electrodynamic model. The magnetic field data from Tirunelveli and Alibag are provided by the Indian Institute of Geomagnetism. The authors thank Dr. Michela Ravanelli for her valuable support. The authors are grateful to Luigi (Gg) Ciraolo at the Abdus Salam International Center for Theoretical Physics for proving the software for TEC calibration and his valuable help about it.

References

Aa, E., Huang, W., Liu, S., Ridley, A., Zou, S., Shi, L., et al. (2018). Midlatitude plasma bubbles over China and adjacent areas during a magnetic storm on 8 September 2017. *Space Weather*, *16*, 321–331. https://doi.org/10.1002/2017SW001776

Aa, E., Zou, S., Ridley, A. J., Zhang, S.-R., Coster, A. J., Erickson, P. J., et al. (2019). Merging of storm time midlatitude traveling ionospheric disturbances and equatorial plasma bubbles. *Space Weather*, *17*, 285–298. https://doi.org/10.1029/2018SW002101

Aarons, J. (1991). The role of the ring current in the generation or inhibition of equatorial F layer irregularities during magnetic storms. *Radio Science*, *26*(04), 1131–1149. https://doi.org/10.1029/91RS00473

Abdu, M. A. (2012). Equatorial spread F/plasma bubble irregularities under storm time disturbance electric fields. *Journal of Atmospheric and Solar-Terrestrial Physics*, *75–76*, 44–56.

Abdu, M. A. (2019). Day-to-day and short-term variabilities in the equatorial plasma bubble/spread F irregularity seeding and development. *Progress in Earth and Planetary Science*, *6*(1), 11. https://doi.org/10.1186/s40645-019-0258-1

Alfonsi, L., Spogli, L., Tong, J. R., De Franceschi, G., Romano, V., Bourdillon, A., & Mitchell, C. N. (2011). GPS scintillation and TEC gradients at equatorial latitudes in April 2006. *Advances in Space Research*, *47*(10), 1750–1757. https://doi.org/10.1016/j.asr.2010.04.020

Basu, S., Basu, S., Valladares, C. E., Yeh, H. C., Su, S. Y., MacKenzie, E., & Groves, K. M. (2001). Ionospheric effects of major magnetic storms during the International Space Weather Period of September and October 1999: GPS observations, VHF/UHF scintillations, and in situ density structures at middle and equatorial latitudes. *Journal of Geophysical Research*, *106*(A12), 30389–30413. https://doi.org/10.1029/2001JA001116

Biktash, L. Z. (2004). Role of the magnetospheric and ionospheric currents in the generation of the equatorial scintillations during geomagnetic storms. *Annales Geophysicae*, *22*, 3195–3202. https://doi.org/10.5194/angeo-22-3195-2004

Booker, H. G., & Wells, H. W. (1938). Scattering of radio waves in the F region of ionosphere. *Terrestrial Magnetism and Atmospheric Electricity*, *43*, 249.

Bornmann, P. L., Speich, D., Hirman, J., Matheson, L., Grubb, R., Garcia, H., & Viereck, R. (1996). "GOES x-ray sensor and its use in predicting solar-terrestrial disturbances," GOES-8 and beyond. In E. R. Washwell (Ed.), Proceedings of SPIE (Vol. 2812, pp. 291–298). https://doi.org/10.1117/12.254076

Bougard, B., Sleewaegen, J. M., Spogli, L., Veettil, S. V., & Monico, J. F. (2011). *CIGALA: Challenging the solar maximum in Brazil with PolaRxS*. 24th International Technical Meeting of the Satellite Division of the Institute of Navigation 2011, ION GNSS 2011 (pp. 2572–2579).

Cesaroni, C., Spogli, L., Alfonsi, L., De Franceschi, G., Ciraolo, L., Monico, J. F. G., & Bougard, B. (2015). L-band scintillations and calibrated total electron content gradients over Brazil during the last solar maximum. *Journal of Space Weather and Space Climate*, *5*, A36. https://doi.org/10.1051/swsc/2015038

Chakraborty, S., Baker, J. B. H., Ruohoniemi, J. M., Kunduri, B. S. R., Nishitani, N., & Shepherd, S. G. (2019). A study of SuperDARN response to co-occurring space weather phenomena. *Space Weather*, *17*, 1351–1363. https://doi.org/10.1029/2019SW002179

Ciraolo, L., Azpilicueta, F., Brunini, C., Meza, A., & Radicella, S. M. (2007). Calibration errors on experimental slant total electron content (TEC) determined with GPS. *Journal of Geodesy*, *81*(2), 111–120. https://doi.org/10.1007/s00190-006-0093-1

Eccles, J. V., St. Maurice, J. P., & Schunk, R. W. (2015). Mechanisms underlying the prereversal enhancement of the vertical plasma drift in the low-latitude ionosphere. *Journal of Geophysical Research: Space Physics*, *120*(6), 4950–4970. https://doi.org/10.1002/2014JA020664

Fejer, B. G. (1991). Low latitude electrodynamic plasma drifts: A review. *Journal of Atmospheric and Terrestrial Physics*, *53*(8), 677–693. https://doi.org/10.1016/0021-9169(91)90121-M

Fremouw, E. J., Leadabrand, R. L., Livingston, R. C., Cousins, M. D., Rino, C. L., Fair, B. C., & Long, R. A. (1978). Early results from the DNA Wideband satellite experiment—Complex-signal scintillation. *Radio Science*, *13*(1), 167–187. https://doi.org/10.1029/RS013i001p00167

Ghobadi, H., Spogli, L., Alfonsi, L., Cesaroni, C., Cicone, A., Linty, N., & Cafaro, M. (2020). Disentangling ionospheric refraction and diffraction effects in GNSS raw phase through fast iterative filtering technique. *GPS Solutions*, *24*(3), 1–13.

Goswami, S., Paul, A., & Haldar, S. (2018). Study of relative performance of different navigational satellite constellations under adverse ionospheric conditions. *Space Weather*, *16*, 667–675. https://doi.org/10.1029/2017SW001762

Jin, H., Zou, S., Chen, G., Yan, C., Zhang, S., & Yang, G. (2018). Formation and evolution of low-latitude F region field-aligned irregularities during the 7–8 September 2017 storm: Hainan coherent scatter phased array radar and digisonde observations. *Space Weather*, *16*, 648–659. https://doi.org/10.1029/2018SW001865

Laken, B. A., & Čalogović, J. (2013). Composite analysis with Monte Carlo methods: An example with cosmic rays and clouds. *Journal of Space Weather and Space Climate*, *3*, A29. https://doi.org/10.1051/swsc/2013051

Laundal, K. M., & Richmond, A. D. (2017). Magnetic coordinate systems. *Space Science Reviews*, *204*, 27–59. https://doi.org/10.1007/s11214-016-0275-y

Li, G., Ning, B., Otsuka, Y., Abdu, M. A., Abadi, P., Liu, Z., & Wan, W. (2020). Challenges to equatorial plasma bubble and ionospheric scintillation short-term forecasting and future aspects in east and southeast Asia. *Surveys in Geophysics*, 1–38. https://doi.org/10.1007/s10712-020-09613-5

Linty, N., Minetto, A., Dovis, F., & Spogli, L. (2018). Effects of phase scintillation on the GNSS positioning error during the September 2017 storm at Svalbard. *Space Weather*, *16*(9), 1317–1329. https://doi.org/10.1029/2018SW001940

Ma, G., & Maruyama, T. (2006). A super bubble detected by dense GPS network at east Asian longitudes. *Geophysical Research Letters*, *33*(21), L21103. https://doi.org/10.1029/2006GL027512

MacDougall, J. W. (1969). The equatorial ionospheric anomaly and the equatorial electrojet. *Radio Science*, *4*(9), 805–810. https://doi.org/10.1029/RS004i009p00805

Mannucci, A. J., Wilson, B. D., Yuan, D. N., Ho, C. H., Lindqwister, U. J., & Runge, T. F. (1998). A global mapping technique for GPS-derived ionospheric total electron content measurements. *Radio Science*, *33*(3), 565. https://doi.org/10.1029/97RS02707

Manoj, C., Lühr, H., Maus, S., & Nagarajan, N. (2006). Evidence for short spatial correlation lengths of the noontime equatorial electrojet inferred from a comparison of satellite and ground magnetic data. *Journal of Geophysical Research*, *111*, A11312. https://doi.org/10.1029/2006JA011855

Manoj, C., Maus, S., Lühr, H., & Alken, P. (2008). Penetration characteristics of the interplanetary electric field to the daytime equatorial ionosphere. *Journal of Geophysical Research*, *113*(A12). https://doi.org/10.1029/2008JA013381

Manoj, C., & Maus, S. (2012). A real-time forecast service for the ionospheric equatorial zonal electric field. *Space Weather*, *10*(9). https://doi.org/10.1029/2012SW000825

Manoj, C., Maus, S., & Alken, P. (2013). Long-period prompt-penetration electric fields derived from CHAMP satellite magnetic measurements. *Journal of Geophysical Research: Space Physics*, *118*(9), 5919–5930. https://doi.org/10.1002/jgra.50511

Martinis, C. R., Mendillo, M. J., & Aarons, J. (2005). Toward a synthesis of equatorial spread F onset and suppression during geomagnetic storms. *Journal of Geophysical Research*, *110*, A07306. https://doi.org/10.1029/2003JA010362

Okabe, A., Boots, B., & Sugihara, K. (1994). Nearest neighbourhood operations with generalized Voronoi diagrams: a review. *International Journal of Geographical Information Systems*, *8*(1), 43–71. https://doi.org/10.1080/02693799408901986

Pi, X., Mannucci, A. J., Lindqwister, U. J., & Ho, C. M. (1997). Monitoring of global ionospheric irregularities using the worldwide GPS network. *Geophysical Research Letters*, *24*(18), 2283–2286. https://doi.org/10.1029/97GL02273

Pritchard, M., Owen, S., Anandakrishnan, S., Holt, W., Bennett, R., La Femina, P., & Stein, S. (2012). Open access to geophysical data sets requires community responsibility, Eos. *Transactions - American Geophysical Union*, *93*(26), 243. https://doi.org/10.1029/2012EO2600

Prölss, G. W. (1995). Ionospheric F-region storms. In H. Volland (Ed.), Handbook of Atmospheric electrodynamics (Vol. 2, pp. 195–248). CRC Press. chap. 8.

Rastogi, R. G., & Klobuchar, J. A. (1990). Ionospheric electron content within the equatorial F2-layer anomaly belt. *Journal of Geophysical Research*, *95*(A11), 19045–19052. https://doi.org/10.1029/JA095iA11p19045

Rastogi, R. G., Rao, D. R. K., Alex, S., Pathan, B. M., & Sastry, T. S. (1997). An intense SFE and SSC event in geomagnetic H, Y and Z fields at the Indian chain of observatories. *Annales Geophysicae*, *15*, 1301. https://doi.org/10.1007/s00585-997-1301-x

Rastogi, R. G., Pathan, B. M., Rao, D. R. K., Sastry, T. S., & Sastri, J. H. (1999). Solar flare effects on the geomagnetic elements during normal and counter electrojet periods. *Earth Planets and Space*, *51*, 947.

Ravanelli, M., Foster, J., & Crespi (2020). *Mattia "TIDs detection from ship-based GNSS receiver: First test on 2010 Maule Tsunami" 2020 IEEE Int. Geosci. Remote Se. Symposium. IEEE*.

Regi, M., Del Corpo, A., & De Lauretis, M. (2016). The use of the empirical mode decomposition for the identification of mean field aligned reference frames. *Annales Geophysicae*, *59*, 6. https://doi.org/10.4401/ag-7067

Regi, M., Redaelli, G., Francia, P., & De Lauretis, M. (2017). ULF geomagnetic activity effects on tropospheric temperature, specific humidity, and cloud cover in Antarctica, during 2003–2010. *Journal of Geophysical Research: Atmospheres*, *122*(12), 6488–6501. https://doi.org/10.1002/2017JD027107

Richmond, A. D. (1995). Ionospheric electrodynamics using magnetic apex coordinates. *Journal of Geomagnetism and Geoelectricity*, *47*, 191–212. https://doi.org/10.5636/jgg.47.191

Savastano, G., Komjathy, A., Verkhoglyadova, O., Mazzoni, A., Crespi, M., Wei, Y., & Mannucci, A. J. (2017). Real-time detection of tsunami ionospheric disturbances with a stand-alone GNSS receiver: A preliminary feasibility demonstration. *Scientific Reports*, *7*, 46607. https://doi.org/10.1038/srep46607

Scherliess, L., & Fejer, B. G. (1997). Storm time dependence of equatorial disturbance dynamo zonal electric fields. *Journal of Geophysical Research*, *102*(A11), 24037–24046. https://doi.org/10.1029/97JA02165

Shreedevi, P. R., Thampi, S. V., Chakrabarty, D., Choudhary, R. K., Pant, T. K., Bhardwaj, A., & Mukherjee, S. (2016). On the latitudinal changes in ionospheric electrodynamics and composition based on observations over the 76–77°E meridian from both hemispheres during a geomagnetic storm. *Journal of Geophysical Research: Space Physics*, *121*. https://doi.org/10.1002/2015JA021841

Tassev, Y., Velinov, P. I. Y., Tomova, D., & Mateev, L. (2017). Analysis of extreme solar activity in early September 2017: G4 – severe geomagnetic storm (07÷08.09) and GLE72 (10.09) in solar minimum. *Comptes rendus de l'Acadèmie bulgare des Sciences*, *70*(10), 1437–1444.

Tsunoda, R. T. (1980). Backscatter measurements of 11- cm equatorial spread-F irregularities. *Geophysical Research Letters*, *7*(10), 848–850. https://doi.org/10.1029/GL007i010p00848

Van Dierendonck, A. J., Klobuchar, J., & Hua, Q. (1993). Ionospheric scintillation monitoring using commercial single frequency C/A code receivers. *Proceedings of ION GPS*, *93*, 1333–1342.

Vanlommel, P., & Van der Linden, R. (2017). STCE newsletter 4 Sep 2017 – 10 Sep 2017, published by the Solar-Terrestrial Centre of Excellence (STCE), issue: 15 Sep 2017. http://www.stce.be/newsletter/

VanZandt, T. E., Clark, W. L., & Warnock, J. M. (1972). Magnetic apex coordinates: A magnetic coordinate system for the ionospheric F2 layer. *Journal of Geophysical Research*, *77*, 2406–2411. https://doi.org/10.1029/JA077i013p02406

Villante, U., & Regi, M. (2008). Solar flare effect preceding Halloween storm (28 October 2003): Results of a worldwide analysis. *Journal of Geophysical Research*, *113*, A00A05. https://doi.org/10.1029/2008JA013132

Weimer, D. R. (2005a). Improved ionospheric electrodynamic models and application to calculating Joule heating rates. *Journal of Geophysical Research*, *110*, A05306. https://doi.org/10.1029/2004JA010884

Weimer, D. R. (2005b). Predicting surface geomagnetic variations using ionospheric electrodynamic models. *Journal of Geophysical Research*, *110*, A12307. https://doi.org/10.1029/2005JA011270

Yang, Z., & Liu, Z. (2016). Correlation between ROTI and ionospheric scintillation indices using Hong Kong low-latitude GPS data. *GPS Solutions*, *20*(4), 815–824. https://doi.org/10.1007/s10291-015-0492-y

Zakharenkova, I., Astafyeva, E., & Cherniak, I. (2016). GPS and in situ Swarm observations of the equatorial plasma density irregularities in the topside ionosphere. *Earth Planets and Space*, *68*(1), 1–11. https://doi.org/10.1186/s40623-016-0490-5